



Pt and Au/TiO₂ photocatalysts for methanol reforming: Role of metal nanoparticles in tuning charge trapping properties and photoefficiency

Alberto Naldoni^a, Massimiliano D'Arienzo^{b,**}, Marco Altomare^c, Marcello Marelli^a, Roberto Scotti^b, Franca Morazzoni^b, Elena Selli^{a,c,***}, Vladimiro Dal Santo^{a,*}

^a CNR – Istituto di Scienze e Tecnologie Molecolari and ERIC Laboratory of “Catalytic materials for hydrogen production”, Via Golgi 19, 20133 Milano, Italy

^b Department of Materials Science, University of Milano-Bicocca, Via R. Cozzi 53, 20125 Milano, Italy

^c Dipartimento di Chimica, Università degli Studi di Milano, Via Golgi 19, 20133 Milano, Italy

ARTICLE INFO

Article history:

Received 10 September 2012

Received in revised form 26 October 2012

Accepted 1 November 2012

Available online 16 November 2012

Keywords:

Photocatalytic hydrogen production

Titanium dioxide

Gold

Platinum

ESR

Charge trapping centers

ABSTRACT

Metal-loaded TiO₂ is, by far, one of the most important class of photocatalysts in hydrogen production through photoreforming of organics and water photosplitting. In this study anatase loaded with Au and Pt nanoparticles (Au/TiO₂ and Pt/TiO₂) by an impregnation-reduction method was investigated as for morphological, electronic (XPS) and photocatalytic properties in hydrogen production by methanol photoreforming. The electron and hole trapping centers, Ti³⁺ and O[•], respectively, formed under UV–vis irradiation of the photocatalysts, were studied by in situ electron spin resonance (ESR) spectroscopy. The nature of the loaded metal affected both the H₂ evolution rate and the distribution of the methanol oxidation products. The better performance of Pt/TiO₂ is attributable to the greater ability of Pt with respect to Au to act as electron sink, slowing the recombination of photogenerated electron–hole couples. Direct evidence of this effect was obtained by ESR analysis, showing that the amount of Ti³⁺ active sites follows the order TiO₂ > Au/TiO₂ >> Pt/TiO₂, thus confirming easier electron transfer from Ti³⁺ to Pt, where the H⁺ reduction to H₂ occurs.

© 2012 Elsevier B.V. All rights reserved.

1. Introduction

Hydrogen generation from biomass and/or water represents a sustainable option for the future energy economy [1,2]. Photocatalytic and photoelectrochemical water splitting as well as photoreforming of organics are viable solutions for small and medium-size scale hydrogen production [3–5]. Although a large number of materials potentially suitable for photo(electro)catalytic hydrogen production have been recently explored, mainly based on semiconductor oxides [6,7], sulphides [8], nitrides [9], oxysulphides [10], and oxynitrides [11], titanium dioxide (TiO₂) is still the benchmark photocatalytic material due to its large availability, cheapness, stability, and non-toxicity. Nevertheless, its wide band gap allows appreciable photoactivity only under UV light

irradiation and the fast electron (e[−])–hole (h⁺) recombination, common to all semiconducting materials, lowers the photocatalytic efficiency.

The availability and separation of photogenerated charges in the photocatalytic material are indeed key issues, which can be improved either (i) by cocatalyst loading (e.g. noble metal, transition-metal oxide, nonmetal-oxide), (ii) by using combinations of semiconductors, or (iii) by modifying the crystal structure and the morphology of the material [12]. Furthermore, the rate of photocatalytic hydrogen production increases also in the presence of sacrificial organic compounds (e.g. methanol [13–17], ethanol, and glycerol [18]), which are able to combine with photogenerated h⁺ more readily than water itself in the photocatalytic splitting of pure water. Although interesting results have been obtained in recent years using approaches (ii) and (iii) [19–21], TiO₂ modified by noble metal nanoparticles (M/TiO₂) still remains the model system for photocatalytic H₂ production [15–17,22,23].

When noble metal nanoparticles (NPs) are loaded onto the surface of TiO₂, photogenerated electrons preferentially migrate from the conduction band of the oxide to the noble metal cocatalyst [24,25], thus decreasing e[−]–h⁺ recombination. Up to now, several metals have been used as titania cocatalyst [26–29] albeit the best performances in the photocatalytic production of H₂ have been obtained with Pt/TiO₂ and Au/TiO₂. The main reason of this behavior relies on the separation of photogenerated charge

* Corresponding author at: CNR – Istituto di Scienze e Tecnologie Molecolari, Via Golgi 19, 20133 Milano, Italy. Tel.: +39 02 50314428; fax: +39 02 50314405.

** Corresponding author. Department of Materials Science, University of Milano-Bicocca, Via R. Cozzi 53, 20125 Milano, 6 Italy. Tel.: +39 0264485400; fax: +39 0264485027.

*** Corresponding author at: Dipartimento di Chimica, Università degli Studi di Milano, Via Golgi 19, 20133 Milano, Italy. Tel.: +39 02 50314237; fax: +39 02 50314300.

E-mail addresses: massimiliano.dariento@mater.unimib.it (M. D'Arienzo), elena.selli@unimi.it (E. Selli), v.dalsanto@istm.cnr.it (V. Dal Santo).

carriers generally attributed to the formation of a Schottky barrier at the metal/TiO₂ interface. The higher is the Schottky barrier, the lower is the recombination rate between the e⁻ transferred to the metal and the h⁺, and the greater the H₂ production [13,15–17,30].

In their early work on the photocatalytic effects of noble metal NPs deposition on TiO₂, Bamwenda et al. [31] reported that the hydrogen yield from water/ethanol solution was greatly improved by Pt deposition on TiO₂, rather than by Au deposition on TiO₂. The higher overall activity of Pt loaded catalysts was ascribed to more effective trapping and pooling of photogenerated electrons on Pt and/or to the higher intrinsic platinum activity in reduction processes.

The literature reports several different methods to load metal NPs onto TiO₂, such as deposition precipitation, impregnation, photoreduction and chemical reduction (with H₂ or NaBH₄) [32]. Among all these methods, the adsorption of noble metal ions onto the titania surface followed by reduction with NaBH₄ produces highly dispersed metal NPs in intimate contact with TiO₂ [32]. Moreover, the obtained M/TiO₂ products exhibit better photocatalytic properties than bare titania, confirming that this technique is suitable to deliver highly active photocatalysts.

Whereas the enhancing effect of loaded noble metals on the photocatalytic properties of TiO₂ in reduction processes is well-established, their action mechanism in the parallel oxidation reactions is still under debate. Furthermore, there is hardly any investigation which directly relates the morphological and electronic properties of the metal co-catalysts to the type, amount and location of the electronic defects and the photoproduced charge carriers active in photocatalytic processes.

Aiming at addressing these points, in the present study the photocatalytic efficiency of Au/TiO₂ and Pt/TiO₂ in hydrogen production from methanol photoreforming has been investigated in relation to the morphological and electronic properties of the photocatalysts, as well as to the charge carriers, detected by electron spin resonance (ESR) spectroscopy in the form of Ti³⁺, O⁻ and O₂⁻ trapping centers, which are photogenerated in the early stage of the photocatalytic process. The direct investigation, performed by ESR analysis, of the paramagnetic species formed under irradiation on TiO₂ has recently provided relevant insight into the mechanism of photocatalytic processes and suggested ways to improve photoefficiency through the manipulation of defect states [33–35].

2. Experimental

2.1. Photocatalysts preparation

A commercial amorphous TiO₂ powder (NanoActive®, NanoScale Co., USA) was used as starting material. It was first kept at 473 K under flowing O₂ for 1 h. After cooling down to room temperature, it underwent further oxidation in flowing O₂ at 773 K for 1 h. The sample obtained by this way was labeled TiO₂-A.

Au- and Pt-modified TiO₂ photocatalysts were prepared as it follows. 500 mg of TiO₂-A were suspended in 40 mL of H₂O and sonicated for 20 min. Then, a HAuCl₄ or H₂PtCl₆ water solution was added and the so obtained suspension was stirred for 30 min. Finally, a NaBH₄ solution (10 mg in 10 mL of H₂O) was added dropwise under stirring and allowed to react for 10 min. The product was then centrifuged, washed 3 times with H₂O and dried under vacuum (10⁻⁵ mbar). The so obtained samples were labeled Au/TiO₂ or Pt/TiO₂, respectively. The nominal amount of metal loaded on M/TiO₂ was 1 wt.% in both cases. An aqueous (40 mL) suspension of TiO₂-A (500 mg) was also treated with the NaBH₄ solution under conditions identical to those adopted for noble metals deposition, apart from the addition of the metal precursors, to produce the TiO₂-Rf reference sample.

2.2. Photocatalysts characterization

The actual Pt and Au loadings were determined by ICP-OES (ICAP 6300, Thermo Electron) after microwave digestion of samples in a 3:1 HCl/HNO₃ mixture. The measured Au and Pt loadings were 0.70 ± 0.02 and 0.64 ± 0.02 wt.%, respectively.

X-ray powder diffraction (XRPD) measurements were performed using a Siemens D500 diffractometer operating at 40 kV and 30 mA, with a Cu Kα radiation source. Data were collected using a scan rate of 1.25°/min and a step size of 0.02°.

Nitrogen physisorption measurements at 77 K were carried out with a Quantachrome Autosorb-1 apparatus. The specific surface area (SSA_{BET}, BET method) [36], pore volume (desorption cumulative pore volume, DCPV) and pore size distribution (BJH method) [37] were measured after evacuation at 473 K for 16 h.

High resolution transmission electron microscopy (HRTEM) and high-angle annular dark-field scanning transmission electron microscopy (HAADF-STEM) were employed to determine the morphology and size distribution of metallic NPs supported on TiO₂, using a Zeiss Libra 200FE instrument. The samples were finely ground using an agate mortar and then dispersed in isopropanol in an ultrasonic bath. A drop of the suspension was gently deposited on a holey-carbon film supported on a copper 300 mesh grid. After solvent evaporation, TEM micrographs were taken spanning wide regions of all examined samples in order to provide a truly representative statistical map of the powders. The size distribution of Au and Pt NPs deposited on TiO₂ was calculated by sampling 200 metallic NPs.

The diffuse reflectance (DR) UV–vis spectra of carefully ground powders were recorded with a Thermo Scientific Evolution 600 spectrophotometer, equipped with a diffuse reflectance accessory Praying-Mantis sampling kit (Harrick Scientific Products, USA). A Spectralon® disk was used as reference material.

The X-ray photoelectron spectroscopy (XPS) analyses were performed with a Omicron ESCA+ spectrometer equipped with a spherical capacitor analyzer, 128 channel detector (channeltrons), monochromator, ion gun and an electron flood gun for charge neutralization. The monochromator had an illuminated area of about 1 mm in diameter. All measurements were done with monochromated Al Kα radiation at 300 W. The accuracy of the reported binding energy (BE) was ± 0.1 eV. The sample analysis area was about 1 mm in diameter and the working pressure below 1 × 10⁻⁹ mbar. Detailed scans were recorded for the C 1s, O 1s, Ti 2p, Au 4f and Pt 4f BE regions. No further element was detected. BE values were corrected by assigning the value of 284.6 eV to the C 1s peak of adventitious hydrocarbons. The analysis involved Shirley-type background subtraction and nonlinear least-squares curve fitting, adopting Gaussian–Lorentzian peak shapes and peak area determination by integration. The atomic compositions were evaluated from peak areas using Scofield sensitivity factors, based on the geometric configuration of the apparatus. The experimental uncertainty on the reported atomic composition values was below ± 5%. Depth profiles were obtained by Ar⁺ sputtering at 2.5 kV under an argon partial pressure of ~1 × 10⁻⁸ mbar and a rastered area of 2 mm × 2 mm. Under these conditions the sputtering rate was 20 Å min⁻¹. For each sample, the chemical composition was checked in at least three different areas.

The ESR investigation was performed by a Bruker EMX spectrometer operating at the X-band frequency and equipped with an Oxford cryostat. The nanocrystals were charged into quartz glass tubes connected both to a high vacuum pumping system and to a controlled gas feed (O₂ or N₂ saturated with CH₃OH/H₂O vapors obtained by continuously bubbling the gas into a CH₃OH/H₂O 20 vol.% solution). Irradiation was performed by a UV–vis 150 W Xe lamp (Oriol) on samples in the cavity through an optical fiber (50 cm length, 0.3 cm diameter). Additional

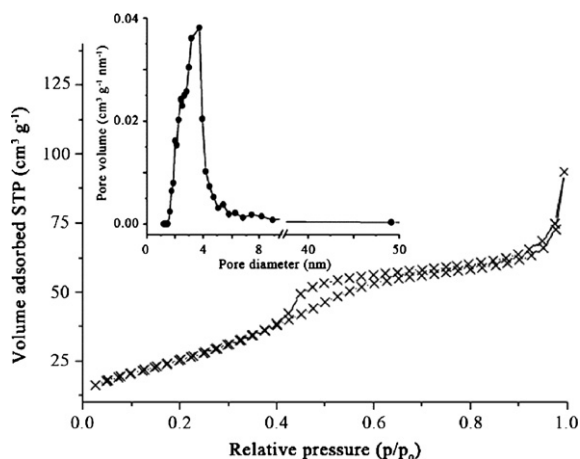


Fig. 1. Adsorption–desorption isotherm at liquid nitrogen temperature for Pt/TiO₂. The curve corresponds to a type IV isotherm with capillary condensation in the mesopores. Inset: pore-size distribution.

experiments were carried out under the same conditions by filtering the UV portion of the lamp emission by a 420 nm cut-off filter. Samples were irradiated at 130 K either in vacuo or in the presence of 10 mbar of O₂ or N₂ saturated with CH₃OH/H₂O. The spectra were recorded at the same temperature in vacuo (10^{−5} mbar) before, during and after 30 min-long irradiation, using a modulation frequency of 100 kHz, modulation amplitudes of 2–5 G and a microwave power of 10 mW.

The *g* values were calculated by standardization with α,α' -diphenyl- β -picryl hydrazyl (DPPH). The spin concentration was obtained by double integration of the resonance lines, referring to the area of the standard Bruker weak pitch ($9.7 \times 10^{12} \pm 5\%$ spins cm^{−1}). Accuracy on double integration was $\pm 15\%$. Care was taken to always keep the most sensitive part of the EPR cavity (1 cm length) filled. Spectra simulations and fits were performed using the SIM 32 program [38]. For each sample, the absence of a signal before irradiation was checked.

2.3. Photocatalytic tests

The photoreactor assembly and experimental conditions employed in photocatalytic hydrogen production tests has already been described in detail elsewhere [39,40]. Briefly, the photocatalyst bed was prepared by mixing 14 mg of photocatalyst powder with 3 g of 20–40 mesh (0.42–0.85 mm) quartz beads and 1.2 mL ultra-pure water, followed by drying in oven at 343 K for 2 h. The photoreactor was connected to a recirculation stainless steel apparatus containing a bubbling system filled with a 20 vol.% CH₃OH aqueous solution. The outlet gas was therefore N₂ saturated by CH₃OH/H₂O vapors, which was then fed to the catalyst bed in the photoreactor. Prior to any run, the whole setup was thoroughly flushed with inert gas in the dark for 30 min, in order to remove any trace of oxygen. The photocatalyst bed was irradiated for 6 h (naked TiO₂ powders) or 2 h (noble metal modified samples). In the latter case, three consecutive irradiation cycles were performed with each photocatalyst bed, with 30 min N₂ purging in the dark between each irradiation cycle. All kinetic tests were repeated three times. The amount of hydrogen produced under irradiation and accumulated in the inert gas was determined by an on line Agilent 6890 N gas-chromatograph, equipped with two columns (HP-PlotU and Molesieve 5A), two detectors (thermo conductivity and flame ionization) and a Ni-catalyst kit for CO and CO₂ methanation, employing N₂ as carrier gas. The irradiation source, always switched on 30 min prior to the beginning of the run, was a Xenon arc lamp (LOT Oriel, 300 W) emitting in the

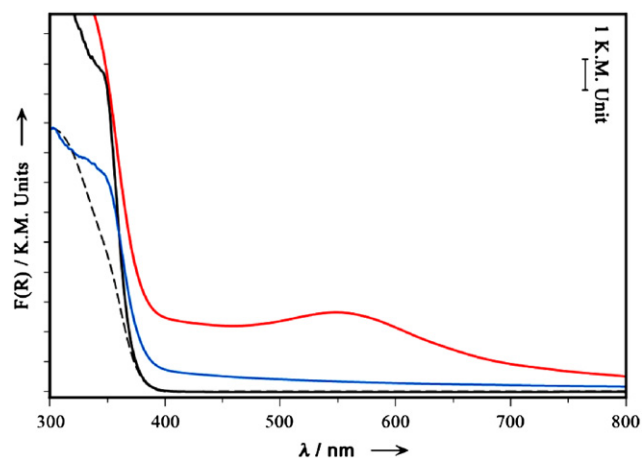


Fig. 2. DR UV–vis spectra of TiO₂-A (black dashed line), TiO₂-Rf (black continuous line), Au/TiO₂ (red line) and Pt/TiO₂ (blue line). (For interpretation of the references to color in this figure legend, the reader is referred to the web version of this article.)

UV–vis range (solar simulator) with a full irradiation intensity of 6.0×10^{-8} einstein s^{−1} cm^{−2} on the reactor, as determined by ferrioxalate actinometry at 308 K.

During the runs H₂, CO₂, and CO accumulated at constant rate in the recirculating gas phase. Their production rates were determined as the slope of the straight lines interpolating their gas phase concentration vs. time plots. The gas-phase concentration of formaldehyde and other minor by-products remained almost constant at the exit of the photoreactor, because they accumulated in the liquid solution. Their average production rates could thus be evaluated from their amount in the aqueous solution at the end of the runs, divided by the overall irradiation time, as already described [13]. The apparent quantum efficiency of H₂ production Φ_{H_2} in the photocatalytic steam reforming of CH₃OH was calculated from the rate of hydrogen production and the measured irradiance on the reactor.

3. Results and discussion

3.1. XRPD analysis

The XRPD pattern of TiO₂-A, reported in Fig. S1 (Supporting Information), shows that the sample was crystalline and contained 100% anatase phase, with 15 nm average crystallite size, evaluated using the Scherrer equation based on the [1 0 1] anatase reflection. Almost identical XRPD patterns were recorded with TiO₂-Rf and with the two metal-loaded samples (not reported), indicating that metal deposition followed by reduction with NaBH₄ did not affect the phase and the crystallite size of the materials.

3.2. Nitrogen physisorption experiments

Nitrogen physisorption experiments were performed on metal-loaded catalysts and on TiO₂-Rf. All samples are mesoporous, showing a type IV Brunauer isotherm. According to the *t*-plot, no micropores were detected. As an example, the adsorption–desorption isotherms and the corresponding monomodal pore-size distribution of Pt/TiO₂ NPs are shown in Fig. 1.

The specific surface areas (*SSA_{BET}*) and BJH pore volumes (*DCPV*) of the different samples are reported in Table 1. It is worth noting that the *SSA_{BET}* of TiO₂-Rf is significantly higher than those of metal-loaded TiO₂. A similar trend is also observed for *DCPV* values, with Au/TiO₂ and Pt/TiO₂ showing 40% and 35% depletion of pore volume in comparison to TiO₂-Rf, respectively. The reduction

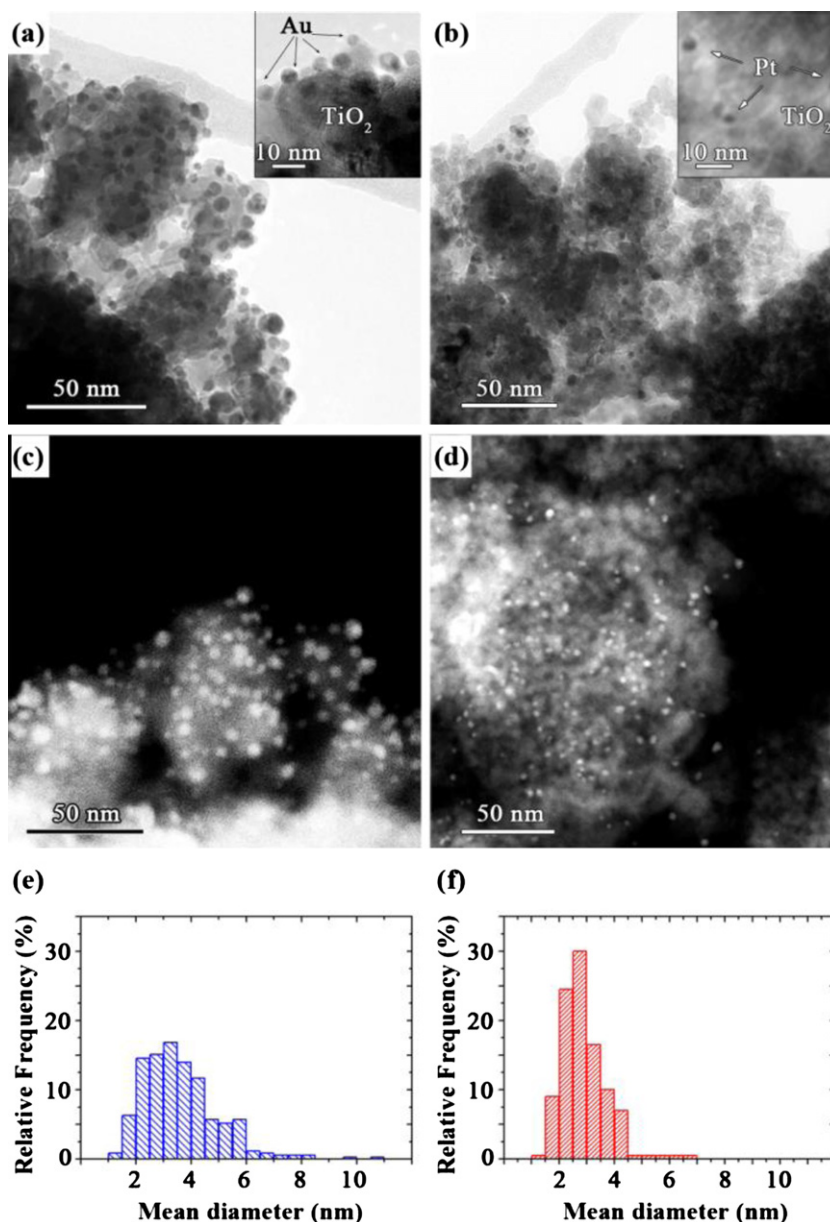


Fig. 3. HRTEM micrographs of (a) Au/TiO₂ and (b) Pt/TiO₂ (the insets are high magnification views of Au and Pt NPs deposited on TiO₂-A crystallites). HAADF-STEM images and metal NPs size distribution of (c and e) Au/TiO₂ and (d and f) Pt/TiO₂, respectively.

in both surface area and in pore volume after metal loading might be a consequence of the deposited metal plugging the pores of the catalyst.

3.3. DR analysis

The DR UV–vis spectra of bare and metal loaded TiO₂ samples are shown in Fig. 2. Diffuse reflectance data were converted into $F(R)$ values according to the Kubelka–Munk equation. TiO₂-Rf showed a bandgap value of ca. 3.1 eV, comparable with those

of TiO₂-A, Au/TiO₂ and Pt/TiO₂, indicating that neither the NaBH₄ treatment nor the metal deposition induced substantial variation of the energy needed for band–band transition.

Au/TiO₂ also shows the typical absorption band ($\lambda_{\text{max}} = 549$ nm) in the visible region attributable to the surface plasmon resonance (SPR) of gold NPs. Differently, the plasmonic absorption of Pt NPs in Pt/TiO₂ is not visible, being covered by the TiO₂ bandgap absorption in the UV spectral region. The weak absorption of Pt/TiO₂ in the visible region has been predicted by theoretical calculations [41].

3.4. HRTEM and HAADF-STEM analyses

The HRTEM micrographs of TiO₂-A and TiO₂-Rf are shown in Fig. S2. Both samples consisted of aggregates of irregular spherical-shaped TiO₂ particles about 10–25 nm in size, in agreement with the calculations based on XRPD analysis, and were composed of well-formed TiO₂ single crystals preferentially exposing the [1 0 1] facets (see fast Fourier transform in the insets of Fig. S2). Thus,

Table 1

Specific surface area SSA_{BET} and total pore volume (DCPV) of bare and metal-loaded titania nanocrystals.

Sample	SSA_{BET} ($\text{m}^2 \text{g}^{-1}$)	BJH pore volume ($\text{cm}^3 \text{g}^{-1}$)
TiO ₂ -Rf	147.9 ± 0.05	0.224
Au/TiO ₂	94.32 ± 0.05	0.135
Pt/TiO ₂	98.11 ± 0.05	0.145

the reduction treatment apparently did not induce any significant modification of the nanomaterial morphology.

The HRTEM and HAADF-STEM images of Au/TiO₂ and Pt/TiO₂ reported in Fig. 3 demonstrate that metal NPs deposited on TiO₂-A via the impregnation/NaBH₄ reduction method were highly dispersed over the whole oxide surface. Both Au (Fig. 3a and c) and Pt (Fig. 3b and d) NPs were grown homogeneously and have spherical shape. The insets in Fig. 3a and b show a high magnification of a typical zone with several Au and Pt NPs on the surface of TiO₂. Based on the HAADF-STEM analysis, the size distribution of Au NPs resulted centered around 3.6 nm (Fig. 3e), that of Pt NPs around 2.9 nm (Fig. 3f). The Pt NPs not only had a lower average diameter compared to Au NPs, but also a narrower size distribution. This peculiarity was proved to be fundamental in influencing the activity of noble metal-loaded photocatalysts (see Section 3.6).

3.5. XPS analysis

XPS analysis was performed on M/TiO₂ samples in order to investigate their electronic properties. In particular, a detailed analysis was performed of the Ti 2p, O 1s, Pt 4f and Au 4f binding energy regions.

A common feature observed for both Au/TiO₂ and Pt/TiO₂ samples is the position of the main ($j = 3/2$) spin-orbit split component of the Ti 2p peak at 458.01 eV, which is typical of Ti(IV) sites coordinated to oxygen atoms (Fig. 4a and c) [42]. Regarding the O 1s peak, a significant broadening and the presence of a shoulder on the high BE side are observed for both samples, suggesting the coexistence of different chemical environments. After peak deconvolution (Fig. 4b and d), the O 1s XPS signal appears to be composed of a major component picking at 529.24 eV, typical of oxygen atoms in the anatase network, and a minor band at higher BE (ca. 530.85 eV) mainly related to the presence of $\equiv\text{Ti}-\text{OH}$ species and/or to some surface hydration [43]. In line with this attribution, the O/Ti atomic ratio,

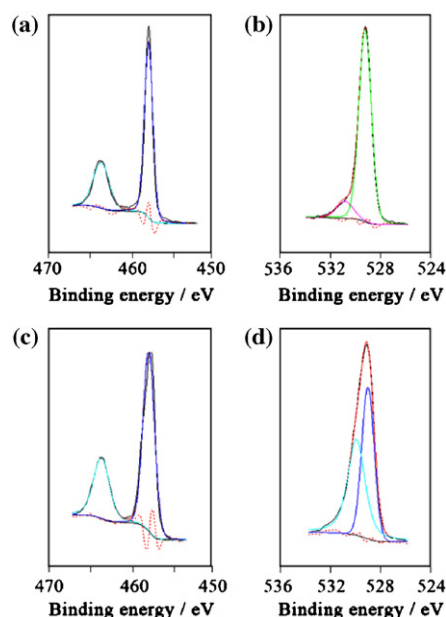


Fig. 4. XPS (a and c) Ti 2p and (b and d) O 1s regions of (a and b) Au/TiO₂ and (c and d) Pt/TiO₂, respectively.

obtained from the XPS survey analysis, was ca. 2.9 for both samples, which is higher than the stoichiometric value (i.e. 2) expected for the oxide.

The in depth XPS analysis reveals a decrease in intensity of the O 1s signals, without any shift of the XPS band maximum during sputtering. By contrast, the Ti 2p signals decrease in intensity and shift to lower BE values, indicating the reduction of Ti(IV) to Ti(III) due to Ar⁺ ion sputtering, as reported in the literature [23]. The Ti atomic concentration depth profile is reported in Fig. S3.

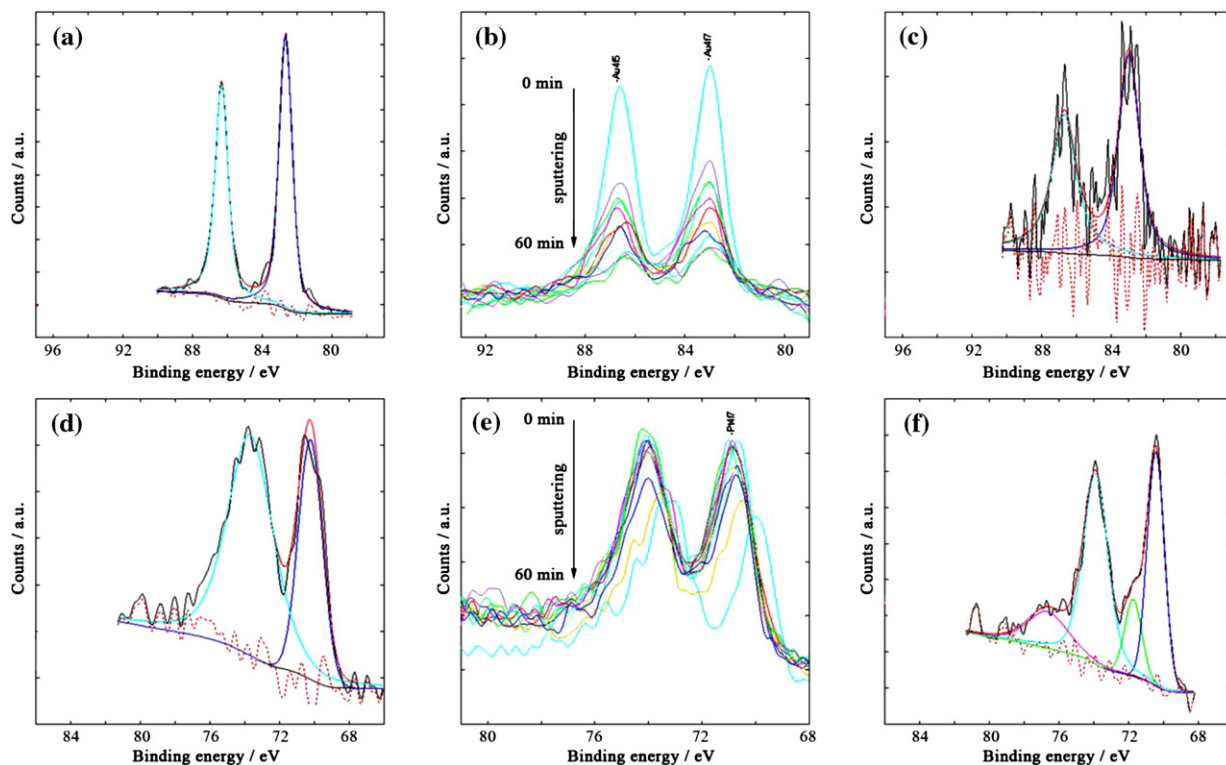


Fig. 5. XPS spectra of the Au 4f region for Au/TiO₂-A (a) before and (c) after 60 min of Ar⁺ sputtering; Pt 4f region for Pt/TiO₂ (d) before and (f) after 60 min of Ar⁺ sputtering; time evolution of the XPS signal in (b) the Au 4f region and (e) the Pt 4f region, after successive steps of Ar⁺ sputtering.

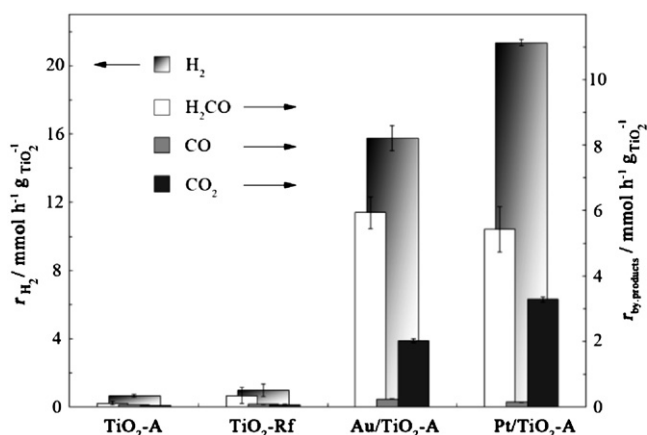


Fig. 6. Hydrogen, formaldehyde, carbon monoxide and carbon dioxide production rates on the investigated photocatalysts during the photocatalytic steam reforming of methanol.

Fig. 5 shows the Au 4f and Pt 4f lines of Au/TiO₂ and Pt/TiO₂, before and after 60 min of Ar⁺ sputtering. The variations in line shape during sputtering are reported in Fig. 5b and e. The shape and peak position of the Au 4f signal (Fig. 5a) (BE Au 4f_{7/2} ≈ 82.72 eV, j–j doublet separation ≈ 3.6 eV) indicate that the metal was dispersed on the titanium oxide surface in metallic Au(0) form only. No changes in the gold electronic state were observed after Ar⁺ sputtering (Fig. 5b and c). The surface Au/Ti atomic ratio was ca. 0.014, in agreement with the nominal noble metal amount.

On the other hand, variations of the Pt 4f peak position were observed, depending on surface etching. In fact, before sputtering, only the Pt(0) species (BE Pt 4f_{7/2} ≈ 70.25 eV, j–j doublet separation of ca. 3.5 eV) was detected by XPS analysis (Fig. 5d). After Ar⁺ sputtering, besides Pt(0), a different oxidized platinum species (BE Pt 4f_{7/2} ≈ 71.72 eV, j–j doublet separation ca. 4.9 eV) appeared (Fig. 5e and f), attributable to the presence of Pt(II) located in the sub-surface region of the Pt NPs [43], with a relative Pt(II)/Pt(0) atomic ratio of ca. 0.2. The surface Pt/Ti atomic ratio was ca. 0.009 in the Pt/TiO₂ sample.

3.6. Hydrogen production by photo-steam reforming

The rate of hydrogen production r_{H_2} during the photocatalytic steam reforming of methanol under the here adopted irradiation conditions is reported in Fig. 6, together with the formation rates of the main methanol oxidation products, i.e. carbon dioxide (CO₂), carbon monoxide (CO) and formaldehyde (H₂CO). Photoactivity greatly increased in the presence of noble metal NPs deposited on the TiO₂ surface, with an increase of the r_{H_2} values by more than one order of magnitude (see Table S1). However, the comparison between the activity results obtained with sample TiO₂-Rf and those obtained with TiO₂-A evidences that also the reducing and cleaning treatment with the NaBH₄ solution contributed in increasing the performance of the bare TiO₂ surface. Thus, in order to discriminate the effects of noble metal NPs on the oxide surface from those induced by TiO₂ modifications consequent to the deposition treatment, TiO₂-Rf should be taken as reference material when discussing the effects of noble metal NPs on the photocatalyst performance. Moreover, platinum confirmed to be a better co-catalyst than gold, as already found in previous studies on the same photocatalytic reaction performed under UV light with a series of noble metal-modified TiO₂ photocatalysts, prepared either by deposition of surfactant-stabilized noble metal NPs or by flame spray pyrolysis in one step [13]. The apparent quantum efficiencies in hydrogen production obtained in the present work with Au/TiO₂ and Pt/TiO₂ under sun simulating light were 10 and

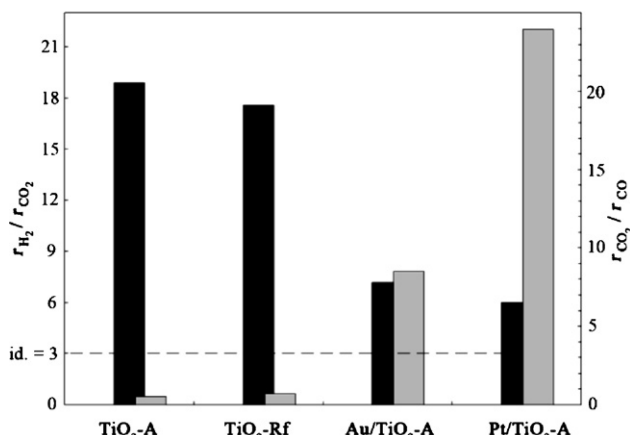


Fig. 7. Ratios between the production rate of H₂ and the production rate of CO₂ (black) and between the production rate of CO₂ and the production rate of CO (gray) during methanol steam reforming with the investigated photocatalysts.

14%, respectively (Table S1). Remarkably, Au/TiO₂ showed a H₂ production rate of 15.8 mmol h⁻¹ g⁻¹, that is ca. 20% higher than that measured for 1 wt.% Au/TiO₂ (P25 Degussa) with the same photocatalytic set-up [13]. At the same way, our Pt/TiO₂ sample presents a 50% and 15% increase in H₂ production rate compared to 0.5 wt.% Pt/TiO₂ (prepared by flame spray pyrolysis in one step) and 1 wt.% Pt/TiO₂ (P25 Degussa) photoactivity, respectively [13].

The presence in the reaction system of oxidation products other than CO₂ confirms that the photoreforming of methanol proceeds through a rather complex mechanism which involves a series of consecutive intermediate oxidation steps occurring on the photocatalyst surface, each of them yielding one H₂ molecule and differently oxidized carbon-containing molecules, which partly desorb from the photocatalyst surface, without any further oxidation [13,44,45]. The effect induced by the presence of noble metal NPs deposited onto the TiO₂ surface on the distribution of the methanol oxidation products can provide valuable information on the role of the metal NPs co-catalysts in increasing the photocatalysts' performance, particularly in the oxidation path.

In fact, as shown in Fig. 7, the r_{H_2} / r_{CO_2} ratio was always much higher than the value, i.e. 3, expected on the basis of complete methanol oxidation, indicating that this reaction was always far from being complete. However, the r_{H_2} / r_{CO_2} ratio dropped from ca. 20 to values ca. double than 3 in the presence of noble metal NPs on the TiO₂ surface. This effect, slightly more remarkable in the case of Pt/TiO₂, indicates that the presence of noble metal NPs not only improves the photocatalysts' performance in general, possibly due to a better photoproduced charge separation, but also provides surface sites ensuring more efficient adsorption and/or complete oxidation of the carbon-containing species involved in the reaction sequence. It is worth underlining that these positive effects of noble metal NPs on the TiO₂ surface prevail on the photoactivity decrease expected as a consequence of the decreased surface area of the materials upon noble metal NPs deposition (see Table 1).

The r_{CO_2} / r_{CO} ratio obtained in kinetic runs performed with the different photocatalysts is also reported in Fig. 7. This ratio is very important from a practical point of view, i.e. when photocatalytic hydrogen is used as a feed for fuel cells. In fact, carbon monoxide, which most probably forms mainly through formic acid photocatalytic dehydration [13,45], would certainly be the most undesired by-product in hydrogen production by photocatalytic reforming of organics, being a well-known poison of Pt-based catalysts in fuel cells. The r_{CO_2} / r_{CO} ratio was below unity for naked TiO₂ (Fig. 7), indicating a very poor performance of these photocatalysts, but largely increased in the presence of noble metal NPs. Once again it is higher

in the case of Pt/TiO₂, thus testifying an increased oxidation ability of this noble metal-modified photocatalyst.

This can easily be evidenced also by a simple comparison between the effects of the presence of Au or Pt NPs on the rates of hydrogen or carbon dioxide production, taking TiO₂-Rf as reference (see Table S1). In fact, whereas r_{H_2} increased by 16 and 22 times upon TiO₂ modification with Au or Pt NPs, respectively, the corresponding r_{CO_2} values were 40 and 66 times greater. In particular, the superior performance of Pt/TiO₂ photocatalyst can be associated to the small diameter and to the narrow size distribution of Pt nanoparticles which guarantee a better intimate metal/TiO₂ contact [46,47].

3.7. ESR investigation

In order to study how the loaded metal (Au, Pt) affects the amount and location of photogenerated charges (e^- and h^+) and drives the photoactivity of TiO₂-Rf, Au/TiO₂ and Pt/TiO₂, ESR spectra were acquired after UV–vis irradiation at 130 K, either in vacuo ($p < 10^{-5}$ mbar) or in the presence of $p(\text{O}_2) = 10$ mbar. For each sample, the absence of signals before irradiation was proved and no significant differences resulted in the ESR spectra recorded just before and 20 min after switching the light off, apart from a small decrease of the signal intensity.

After irradiation under vacuum all samples show two well separated sets of resonances (Fig. 8a). The higher field signals are attributed to electrons trapped at different Ti³⁺ centers (Ti³⁺ [I] and Ti³⁺ [II] see Table 2) [34,35,42–52]. In detail, the narrow signal at $g = 1.988$, mainly evident in TiO₂-Rf and Au/TiO₂, is attributable to the perpendicular g -tensor component of anatase Ti³⁺ bulk centers (Ti³⁺ [I], the corresponding g_{\parallel} resonance being not detectable due to the overlap with the other resonance lines). The about symmetrical broad resonances of Ti³⁺ [II] are assigned to Ti³⁺ sites located in a disordered environment and probably near the surface [52]. The lower field features can be attributed to superimposed oxygen species, O^{•−} and O₂^{•−} [32,53,54], whose g values and relative amounts were calculated by signal simulation (Fig. 8a and Table 2). In particular, the lower field resonances occurring in Pt/TiO₂ were reproduced by five different components (Fig. 8b and Table 2): two overlapping axial species due to h^+ trapped at two distinct O^{•−} sites (O^{•−} [I] and O^{•−} [II]) and three orthorhombic species assigned to superoxide anions with different g_{zz} values (O₂^{•−} [I], O₂^{•−} [II] and O₂^{•−} [III]).

The differences in the g_{zz} component indicate that several cationic surface sites are available for the stabilization of the superoxide radical. According to the ionic model originally proposed by Kanzig and Cohen for bulk halides [55], the g_{zz} component is largely sensitive to the electric field generated by the metal cation of the adsorption site. In the case of TiO₂ the value is indicative of slight changes in Ti³⁺ charge, generated by different surrounding groups (e.g. metal loaded on the surface).

The presence of O₂^{•−} species, mainly occurring in TiO₂-Rf and Au/TiO₂ nanocrystals, even when UV irradiation was performed under vacuum, may be ascribed to the evolution of residuals OH[−] groups according to the following mechanism [56]:



Due to their significance in evidencing the e^- – h^+ charge separation, the amounts of the O^{•−} species (calculated as percent of the total intensity of the O^{•−} + O₂^{•−} signals by simulation of the normalized spectra) were determined and reported in Table 2 for the different samples.

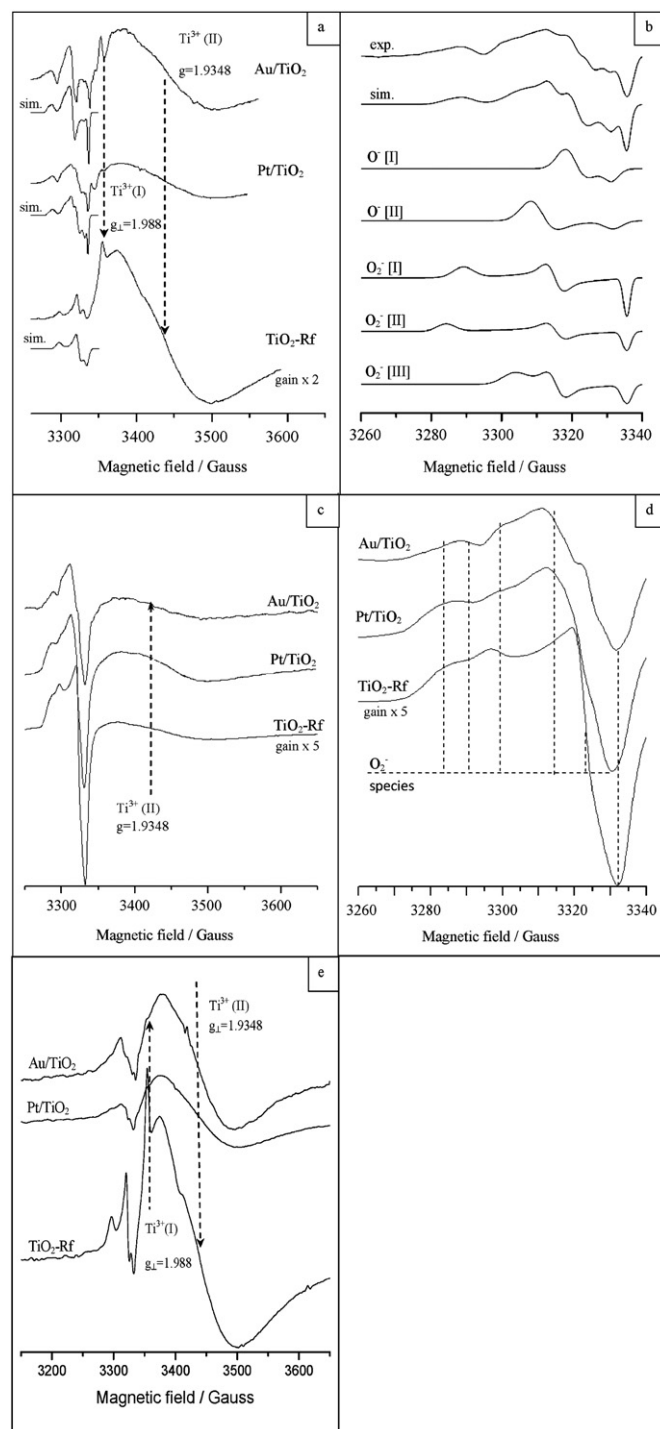


Fig. 8. (a) ESR spectra of bare and metal-loaded anatase at 130 K after UV–vis irradiation in vacuo at $p < 10^{-5}$ mbar. (b) Deconvolution (sim.) of ESR signals of Pt/TiO₂ (exp.) into O^{•−} and O₂^{•−} species. (c) ESR spectra after UV–vis irradiation in the presence of 10 mbar of O₂ and then under vacuum at $p < 10^{-5}$ mbar. (d) Magnification of the O₂^{•−} spectral region. (e) ESR spectra after UV irradiation in the presence of 10 mbar of N₂ (saturated in MeOH/H₂O 20% (v/v) solution) and subsequent evacuation at $p < 10^{-5}$ mbar.

The abundance and the stability of the paramagnetic centers detected by ESR after UV–vis irradiation are relatable to the charge separation, to their inhibited recombination and to the presence of metal or other impurities on the oxide surface [34,35,48–54].

In the present case, Fig. 8a clearly shows that, after irradiation in vacuo, the concentration of e^- trapped on Ti³⁺ sites (in the range 8.4×10^{15} – 1.2×10^{17} spin g^{-1}) always exceeds that of h^+

Table 2
g tensor values of the paramagnetic defects detected after photoexcitation in vacuo ($p < 10^{-5}$ mbar) in bare and metal-loaded TiO₂ nanocrystals determined by simulation of the ESR features along with the relative contribution of the O^{•−} species (calculated as percent of the total intensity of the O^{•−} + O₂^{•−} signals, after spectra normalization).

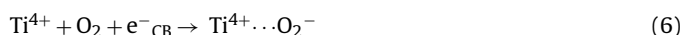
Sample	O ^{•−} (%)	O ^{•−} species	Ti ³⁺ species	O ₂ ^{•−} species
TiO ₂ -Rf	4.5	O ^{•−} : $g_{\perp} = 2.0080$, $g_{\parallel} = 2.0016$	Ti ³⁺ [I]: $g_{\perp} = 1.9880$, $g_{\parallel} = \text{n.d.}$ Ti ³⁺ [II]: $g_{\perp} = 1.9348$, $g_{\parallel} = 1.9045$	O ₂ ^{•−} : $g_{zz} = 2.0233$, $g_{yy} = 2.0094$, $g_{xx} = 2.0003$
Au/TiO ₂	5.7	O ^{•−} [I]: absent O ^{•−} [II]: $g_{\perp} = 2.0153$, $g_{\parallel} = 2.0023$	Ti ³⁺ [I]: $g_{\perp} = 1.9880$, $g_{\parallel} = \text{n.d.}$ Ti ³⁺ [II]: $g_{\perp} = 1.9348$, $g_{\parallel} = 1.9045$	O ₂ ^{•−} [I]: $g_{zz} = 2.0282$, $g_{yy} = 2.0121$, $g_{xx} = 2.0000$ O ₂ ^{•−} [II]: $g_{zz} = 2.0312$, $g_{yy} = 2.0121$, $g_{xx} = 2.0000$ O ₂ ^{•−} [III]: $g_{zz} = 2.0194$, $g_{yy} = 2.0121$, $g_{xx} = 2.0000$
Pt/TiO ₂	16.8	O ^{•−} [I]: $g_{\perp} = 2.0095$, $g_{\parallel} = 2.0023$ O ^{•−} [II]: $g_{\perp} = 2.0153$, $g_{\parallel} = 2.0023$	Ti ³⁺ [I]: $g_{\perp} = 1.9880$, $g_{\parallel} = \text{n.d.}$ Ti ³⁺ [II]: $g_{\perp} = 1.9348$, $g_{\parallel} = 1.9045$	O ₂ ^{•−} [I]: $g_{zz} = 2.0282$, $g_{yy} = 2.0121$, $g_{xx} = 2.0000$ O ₂ ^{•−} [II]: $g_{zz} = 2.0312$, $g_{yy} = 2.0121$, $g_{xx} = 2.0000$ O ₂ ^{•−} [III]: $g_{zz} = 2.0194$, $g_{yy} = 2.0121$, $g_{xx} = 2.0000$

trapped on O^{•−} (1×10^{13} – 7.1×10^{13} spin g^{−1}). In detail, the highest amount of Ti³⁺ centers is detected in TiO₂-Rf nanocrystals, while it decreases in Au/TiO₂ becoming the lowest in Pt-loaded TiO₂ (Table 3). In the first case photogenerated electrons remain at the TiO₂ surface promoting the reaction but also undergoing recombination with h⁺. Otherwise, when Au or Pt are added, photogenerated electrons are readily transferred to the noble metal NPs and particularly to the Pt ones anchored on TiO₂ surface [24], becoming less available to both charge trapping onto Ti³⁺ species and recombination with h⁺. Indeed, electron trapping by Pt decreases the charge recombination rate and therefore favors the hole trapping by O₂^{•−}, as assessed by the higher amount of O^{•−} species detected in Pt/TiO₂ samples compared to Au/TiO₂ and TiO₂-Rf (see Table 2). Therefore, loaded metals act as an electron ‘sink’, with Pt being much more efficient than Au, probably due to the larger difference between its work function ϕ and that of TiO₂ ($\Delta\phi_{\text{Pt-TiO}_2} = 1.5$ vs. $\Delta\phi_{\text{Au-TiO}_2} = 0.7$ eV) [57,58]. As a consequence, the e[−]–h⁺ recombination events in Pt/TiO₂ decrease in comparison with bare TiO₂ and the quantum efficiency for H₂ production (Φ_{H_2} see Table S1) increases by more than one order of magnitude, the electrons on the metal phase being more readily available for H⁺ reduction. The positive oxidation state of some Pt centers, as evidenced by XPS data (Fig. 5f), may also help to drain electrons toward the noble metal, thus supporting the intrinsic electron scavenging action of Pt and improving the charge separation.

The presence of the metal NPs not only affects H₂ production, but also the product distribution in the photocatalytic oxidation of methanol (Fig. 7). In fact, methanol photoreforming on the Au/TiO₂ catalyst gives rise to high amounts of H₂CO and CO, but low CO₂ production. Conversely, Pt/TiO₂ induces the formation of lower amounts of H₂CO and CO and a higher CO₂ production (Fig. 7). Looking at the reaction steps involved in the photocatalytic anaerobic oxidation of methanol in the presence of noble metal-loaded TiO₂ [43], the here obtained performances can be associated to the amount of trapped hole centers (O^{•−} centers), i.e. the higher the amount of h⁺ trapping centers detected by ESR spectroscopy, the higher the amount of fully mineralized carbonaceous products.

The ESR investigation on metal-loaded TiO₂ was performed after UV–vis irradiation at 130 K also in the presence of $p(\text{O}_2) = 10$ mbar and subsequent removal of the residual oxygen by evacuation at $p < 10^{-5}$ mbar (Fig. 8c and d). The resonances of Ti³⁺ and of O₂^{•−} centers can be easily detected (Fig. 8a). The formation of superoxide species (evidenced in Fig. 8d) formally involves the transfer of

electrons from both Ti³⁺ sites and the conduction band (e[−]_{CB}) to molecular O₂, as it follows [53]:



According to reaction (5), the intensity of the Ti³⁺ resonances in TiO₂-Rf and Au/TiO₂ after O₂ contact becomes much lower than in vacuo (see Table 3). By contrast, for Pt/TiO₂ the amount of Ti³⁺ centers remains more or less constant. This suggests that superoxide formation in Pt/TiO₂ does not significantly involve Ti³⁺ centers, probably because they lie in a subsurface region.

Recently, the injection of electrons from Au NPs to TiO₂ has been suggested to be active in various photocatalytic processes such as water splitting and aerobic oxidation of alcohols [59,60]. Using excitation wavelengths close to the Au surface plasmon resonance (SPR) band, the collective oscillation of electrons on the Au particles induced by the incident light has been hypothesized to be able to transfer conduction electrons from the Au NPs to the TiO₂ conduction band.

Taking into account that the photoreactivity of Au/TiO₂ could in principle be influenced by this effect, the ESR spectra of Au/TiO₂ at 130 K were recorded under visible light irradiation (cut-off filter at 420 nm), either in vacuo ($p < 10^{-5}$ mbar) or in the presence of $p(\text{O}_2) = 10$ mbar. However, in all experiments no paramagnetic ESR-active species were detected. Thus, although electron transfer cannot in principle be excluded, no electrons were trapped on TiO₂ as paramagnetic Ti³⁺ species under such irradiation condition. Since the contact with O₂ after visible light irradiation also did not evidence any electron transfer from the TiO₂ conduction band to O₂, usually detectable as O₂^{•−}, we conclude that visible light irradiation does not induce any e[−] transfer to the conduction band levels and that SPR absorption in our Au/TiO₂ sample does not contribute to its activation.

Finally, to simulate the condition experienced by TiO₂ samples during the photocatalytic tests (see Section 3.6), TiO₂-Rf, Au/TiO₂ and Pt/TiO₂ underwent UV–vis irradiation at 130 K in the presence of 10 mbar of N₂ saturated in MeOH/H₂O 20% (v/v) solution. After this treatment, the gas excess was removed by evacuation at 10^{-5} mbar, and the ESR spectra were recorded (Fig. 8e). The very complex signal at low magnetic field is due to the superimposition of different species, mainly O^{•−} and O₂^{•−} centers. Regarding the possible presence of hydroxylmethyl

Table 3
Amount of paramagnetic Ti³⁺ traps (spin g^{−1}) detected at 130 K in M/TiO₂ samples and in bare titania after UV–vis irradiation in different conditions.

Sample	Ti ³⁺ species (spin g ^{−1})		
	UV–vis irradiation in vacuo ($p < 10^{-5}$ mbar)	UV–vis irradiation in $p(\text{O}_2) = 10$ mbar	UV–vis irradiation in $p(\text{N}_2 \text{ saturated with MeOH}) = 10$ mbar
TiO ₂ -Rf	1.6×10^{18}	4.5×10^{17}	4.9×10^{18}
Au/TiO ₂	2.4×10^{17}	4.8×10^{16}	4.6×10^{17}
Pt/TiO ₂	1.6×10^{17}	1.6×10^{17}	3.3×10^{17}

radicals ($\cdot\text{CH}_2\text{OH}$) generated by methanol photo-oxidation at the TiO_2 surface, they cannot be detected at $T > 77\text{ K}$ [61,62]. At higher magnetic field, the intensity of Ti^{3+} active sites follows the same trend observed after irradiation in vacuo, $\text{TiO}_2 > \text{Au/TiO}_2 \gg \text{Pt/TiO}_2$, even if a considerable increase in the whole amount of Ti^{3+} traps becomes evident in all the samples (Table 3). These results confirms that methanol, reacting irreversibly with the photogenerated holes, acts as an efficient h^+ scavenger, suppressing the recombination of electrons and holes on the semiconductor surface.

4. Conclusions

In the present study, the catalytic efficiency of Au/TiO_2 and Pt/TiO_2 in H_2 production through photoreforming of methanol was related to their morphological and electronic properties, as well as to the trapping and the reactivity of the charge carriers photo-generated in the early stage of the process. Pt/TiO_2 displays higher activity than Au/TiO_2 and bare TiO_2 , in both hydrogen production and complete methanol oxidation.

ESR investigation evidenced that interfacial transfer and trapping of photogenerated charges are greatly affected by the metal loaded on the titania surface. In particular, after photoexcitation in vacuo, the amount of electron traps, i.e. Ti^{3+} centers, follows the order $\text{TiO}_2 \text{ Rf} \gg \text{Au/TiO}_2 > \text{Pt/TiO}_2$ while that of the hole traps, i.e. O^- centers, shows an opposite trend, being highest in Pt/TiO_2 . Since H_2 production is associated to electron transfer, photogenerated electrons in Pt/TiO_2 are more readily transferred to Pt NPs, where they can easily reduce H^+ centers. This indicates the greater ability of Pt with respect to Au to act as electron sink and is in line with the difference between the Pt work function and that of TiO_2 . This effect may be also associated to the smaller size of Pt NPs with respect to Au NPs, as detected by TEM analysis, which could favor the electron transfer between oxide and metal, improving the charge separation and the catalytic activity. Therefore, by investigating the interfacial reactivity of the charge trapping sites in M/TiO_2 anatase nanocrystals in connection with their morphological and electronic properties we provided an effective way to understand the role of the noble metal in upgrading the efficiency of H_2 production.

Acknowledgements

M.D. gratefully acknowledges Dr. Ulrich Roll and Omicron Nanotechnology for the experimental support in the XPS characterization of the samples. A.N. and M.M gratefully acknowledge grants from the Italian Ministry of Education, University and research (MIUR) through the FIRB project "ItalNanoNet" (RBPR05JH2P). V.D.S. gratefully acknowledges financial support from the Italian Ministry of Education, University and research (MIUR) through the FIRB project "Oxides at the nanoscale: multifunctionality and applications" (RBAP115AYN).

Appendix A. Supplementary data

Supplementary data associated with this article can be found, in the online version, at <http://dx.doi.org/10.1016/j.apcatb.2012.11.006>.

References

- [1] D. Chen, L. He, *ChemCatChem* 3 (2011) 490–511.
- [2] D.B. Levin, R. Chahine, *International Journal of Hydrogen Energy* 35 (2010) 4962–4969.
- [3] D. Barreca, G. Carraro, V. Gombac, A. Gasparotto, C. Maccato, P. Fornasiero, E. Tondello, *Advanced Functional Materials* 21 (2011) 2611–2623.
- [4] Z. Chen, T.F. Jaramillo, T.G. Deutsch, A. Kleiman-Shwarstein, A.J. Forman, N. Gaillard, R. Garland, K. Takanabe, C. Heske, M. Sunkara, E.W. McFarland, K. Domen, E.L. Miller, J.A. Turner, H.N. Dinh, *Journal of Materials Research* 25 (2010) 3–16.
- [5] K. Shimura, H. Yoshida, *Energy and Environmental Science* 4 (2011) 2467–2481.
- [6] F. Zuo, L. Wang, T. Wu, Z. Zhang, D. Borchardt, P. Feng, *Journal of the American Chemical Society* 132 (2010) 11856–11857.
- [7] M. Cargnello, A. Gasparotto, V. Gombac, T. Montini, D. Barreca, P. Fornasiero, *European Journal of Inorganic Chemistry* (2011) 4309–4323.
- [8] J. Zhang, J. Yu, Y. Zhang, Q. Li, J.R. Gong, *Nano Letters* 11 (2011) 3026–3033.
- [9] D. Wang, A. Pierre, G. Kibria, K. Cui, X. Han, K.H. Bevan, H. Guo, S. Paradis, A. Hakima, Z. Mi, *Nano Letters* 11 (2011) 2353–2357.
- [10] A. Ishikawa, T. Takata, J.N. Kondo, M. Hara, H. Kobayashi, K. Domen, *Journal of the American Chemical Society* 124 (2002) 13547–13553.
- [11] M. Higashi, K. Domen, R. Abe, *Journal of the American Chemical Society* 134 (2012) 6968–6971.
- [12] X. Chen, S. Shen, L. Guo, S.S. Mao, *Chemical Reviews* 110 (2010) 6503–6570.
- [13] G.L. Chiarello, M.H. Aguirre, E. Selli, *Journal of Catalysis* 273 (2010) 182–190.
- [14] N. Stratakis, V. Bekiaris, D.I. Kondarides, P. Lianos, *Applied Catalysis B* 77 (2007) 184–189.
- [15] P. Pichat, *New Journal of Chemistry* 11 (1987) 135–140.
- [16] C.-M. Wang, A. Heller, H. Gerischer, *Journal of the American Chemical Society* 114 (1992) 5230–5234.
- [17] O. Rosseler, M.V. Shankar, M. Karkmaz-Le Du, L. Schmidlin, N. Keller, V. Keller, *Journal of Catalysis* 269 (2010) 179–190.
- [18] A. Gallo, T. Montini, M. Marelli, A. Minguzzi, V. Gombac, R. Psaro, P. Fornasiero, *V. Dal Santo, ChemSusChem* 5 (2012) 1800–1811.
- [19] H. Tada, Q. Jin, H. Nishijima, H. Yamamoto, M. Fujishima, S. Okuoka, T. Hattori, Y. Sumida, H. Kobayashi, *Angewandte Chemie International Edition* 50 (2011) 7088–7092.
- [20] X. Chen, L. Liu, P.Y. Yu, S.S. Mao, *Science* 331 (2011) 746–750.
- [21] A. Naldoni, M. Allietta, S. Santangelo, M. Marelli, F. Fabbri, S. Cappelli, C.L. Bianchi, R. Psaro, V. Dal Santo, *Journal of the American Chemical Society* 134 (2012) 7600–7603.
- [22] P. Kamat, *Journal of Physical Chemistry B* 106 (2002) 7729–7744.
- [23] A.L. Linsebigler, G. Lu, J.T. Yates, *Chemical Reviews* 95 (1995) 735–758.
- [24] J.G. Highfield, P. Pichat, *New Journal of Chemistry* 13 (1989) 61–66.
- [25] T. Hirakawa, P.R. Kamat, *Journal of the American Chemical Society* 127 (2005) 3928–3934.
- [26] Z. Zheng, B. Huang, X. Qin, X. Zhang, Y. Daib, M.H. Whangbo, *Journal of Materials Chemistry* 21 (2011) 9079–9087.
- [27] A. Tanaka, S. Sakaguchi, K. Hashimoto, H. Kominami, *Catalysis Science and Technology* 2 (2012) 907–909.
- [28] M. Ni, M.K.H. Leung, D.Y.C. Leung, K. Sumathy, *Renewable and Sustainable Energy Reviews* 11 (2007) 401–425.
- [29] N. Zhang, S. Liu, X. Fu, Y.J. Xu, *Journal of Physical Chemistry C* 115 (2011) 9136–9145.
- [30] A.V. Kozhakov, N.I. Ermokhina, A.L. Stroyuk, V.K. Bukhtiyarov, A.E. Raevskaya, V.I. Litvin, S.Y. Kuchmiy, V.G. Ilyin, P.A. Manorik, *Journal of Photochemistry and Photobiology A* 198 (2008) 126–134.
- [31] G.R. Bamwenda, S. Tsubota, T. Nakamura, M. Haruta, *Journal of Photochemistry and Photobiology A* 89 (1995) 177–189.
- [32] M.V. Dazzi, L. Prati, P. Canton, E. Selli, *Physical Chemistry Chemical Physics* 11 (2009) 7171–7180.
- [33] M. D'Arienzo, J. Carbajo, A. Bahamonde, M. Crippa, S. Polizzi, R. Scotti, L. Wahba, F. Morazzoni, *Journal of the American Chemical Society* 133 (2011) 17652–17661.
- [34] R. Scotti, M. D'Arienzo, A. Testino, F. Morazzoni, *Applied Catalysis B* 88 (2009) 497–504.
- [35] R. Scotti, I.R. Bellobono, C. Canevali, C. Cannas, M. Catti, M. D'Arienzo, A. Musinu, S. Polizzi, M. Sommariva, A. Testino, F. Morazzoni, *Chemistry of Materials* 20 (2008) 4051–4061.
- [36] S. Brunauer, P.H. Emmett, E. Teller, *Journal of the American Chemical Society* 60 (1938) 309–319.
- [37] E.P. Barret, L.G. Joyner, P.P. Halenda, *Journal of the American Chemical Society* 73 (1951) 373–380.
- [38] A. Adamski, T. Spalek, Z. Sojka, *Research on Chemical Intermediates* 29 (2003) 793–804.
- [39] G.L. Chiarello, L. Forni, E. Selli, *Catalysis Today* 144 (2009) 69–74.
- [40] G.L. Chiarello, A. Di Paola, L. Palmisano, E. Selli, *Photochemical and Photobiological Sciences* 10 (2011) 355–360.
- [41] C.L. Muhich, Y. Zhou, A.M. Holder, A.W. Weimer, C.B. Musgrave, *Journal of Physical Chemistry C* 116 (2012) 10138–10149.
- [42] G. Cappelletti, S. Ardisson, C.L. Bianchi, S. Gialanella, A. Naldoni, C. Pirola, V. Ragaini, *Nanoscale Research Letters* 4 (2009) 97–105.
- [43] G. Wang, H. Wang, Y. Ling, Y. Tang, X. Yang, R.C. Fitzmorris, C. Wang, J.Z. Zhang, Y. Li, *Nano Letters* 11 (2011) 3026–3033.
- [44] Z. Liu, B. Guo, L. Hong, H. Jiang, *Journal of Photochemistry and Photobiology A* 172 (2005) 81–88.
- [45] G.L. Chiarello, D. Ferri, E. Selli, *Journal of Catalysis* 280 (2011) 168–177.
- [46] N. Stratakis, N. Boukos, F. Paloukakis, S.G. Neophytides, P. Lianos, *Photochemical and Photobiological Sciences* 8 (2009) 639–643.
- [47] Y. Mizukoshi, Y. Makise, T. Shuto, J. Hu, A. Tominaga, S. Shironita, S. Tanabe, *Ultrasonics Sonochemistry* 14 (2007) 387–392.
- [48] D.C. Hurum, K.A. Gray, T. Rajh, M.C. Thurnauer, *Journal of Physical Chemistry B* 109 (2005) 977–980.
- [49] D.C. Hurum, A.G. Agrios, S.E. Crist, K.A. Gray, T. Rajh, M.C. Thurnauer, *Journal of Electron Spectroscopy* 107 (2006) 155–163.

- [50] D.C. Hurum, A.G. Agrios, K.A. Gray, T. Rajh, M.C. Thurnauer, *Journal of Physical Chemistry B* 107 (2003) 4545–4549.
- [51] T. Berger, M. Sterrer, O. Diwald, E. Knozinger, D. Panayotov, T.L. Thompson, J.T. Yates, *Journal of Physical Chemistry B* 109 (2005) 6061–6068.
- [52] J.E. Elser, T. Berger, M. Sterrer, D. Brandhuber, J. Bernardi, O. Diwald, E. Knozinger, *Journal of Physical Chemistry B* 110 (2006) 7605–7608.
- [53] T. Berger, O. Diwald, E. Knozinger, M. Sterrer, J.T. Yates, *Physical Chemistry Chemical Physics* 8 (2006) 1822–1826.
- [54] E. Carter, A.F. Carley, D.M. Murphy, *The Journal of Physical Chemistry C* 111 (2007) 10630–10638.
- [55] W. Kanzig, M.H. Cohen, *Physical Review Letters* 3 (1959) 509–510.
- [56] R.F. Howe, M. Gratzel, *Journal of Physical Chemistry* 91 (1987) 3906–3909.
- [57] P.C. Rusu, G. Brocks, *Physical Review B* 74 (2006) 073414–073426.
- [58] K. Tvrđy, P.A. Frantsuzov, P.V. Kamat, *Proceedings of the National Academy of Sciences* 108 (2011) 29–34.
- [59] C.G. Silva, R. Juarez, T. Marino, R. Molinari, H. Garcia, *Journal of the American Chemical Society* 133 (2011) 595–602.
- [60] D. Tsukamoto, Y. Shiraishi, Y. Sugano, S. Ichikawa, S. Tanaka, T. Hirai, *Journal of the American Chemical Society* 134 (2012) 6309–6315.
- [61] O.I. Micic, Y. Zhang, K.R. Cromack, A.D. Trifunac, M.C. Thurnauer, *Journal of Physical Chemistry* 97 (1993) 13284–13288.
- [62] I.A. Shkrob, T.W. Marin, H. He, P. Zapol, *Journal of Physical Chemistry C* 116 (2012) 9450–9460.